Chinese Chemical Letters 33 (2022) 1907–1912

Contents lists available at ScienceDirect

Chinese Chemical Letters

journal homepage: www.elsevier.com/locate/cclet

Sonodynamic cancer therapy by novel iridium-gold nanoassemblies

Jiayi Zhu[a,b], Ai Ouyang[a], Zhuanglin Shen[a], Zhihao Pan[a], Samya Banerjee[c], Qianling Zhang[a], Yantao Chen[a], Pingyu Zhang[a,*]

[a] College of Chemistry and Environmental Engineering, Shenzhen University, Shenzhen 518060, China
[b] College of Physics and Optoelectronic Engineering, Shenzhen University, Shenzhen 518060, China
[c] Department of Chemistry, Indian Institute of Technology (BHU), Varanasi, UP 221005, India

ARTICLE INFO

Article history:
Received 16 August 2021
Revised 1 November 2021
Accepted 3 November 2021
Available online 11 November 2021

Keywords:
Metals in medicine
Iridium complex
Sonocatalysis
Sonodynamic therapy
Bioinorganic chemistry

ABSTRACT

Metal-based compounds with excellent photo-physical properties show good photochemotherapeutic performance. But, low in-depth tissue penetration of light limits their effectivity for deeply buried tumors. Encouraged by the sonosensitizing ability of the traditional organic photosensitizers, here, we developed AuNPs@Ir1 as a sonosensitizer by hybridizing an organometallic Ir(III) complex (Ir1) with ultrasmall gold nanoparticles (AuNPs) for efficient tumor sonodynamic therapy (SDT) for the first time. AuNPs@Ir1 rapidly entered the cancer cells, produced $^1O_2$, and catalytically oxidized NADH to NAD^+ under ultrasound (US) irradiation, thus resulted in cancer cells oncosis. Because of efficient passive retention in tumors post intravenous injection, AuNPs@Ir1 further efficiently inhibited the growth of tumors *in-vivo* under US stimulation without long-term toxicity to other organs. Overall, this work presents the excellent US triggered *in-vitro* and *in-vivo* anticancer profile of the novel AuNPs@Ir1. It is expected to increase the scope of SDT for metal-based anticancer drugs.

Cancer is now one of the most common threats to human health and a major global health challenge to overcome [1]. Non-invasive treatment strategies, triggered by external stimuli, have attracted wide attention due to their control way of treatment, significant therapeutic effects, and low damage to normal tissues [2–5]. Light has been used as a stimulus in many therapies for hundreds of years [6]. For example, photodynamic therapy (PDT) has achieved promising attention and therapeutic effects [7–10]. However, low in-depth tissue penetration of light and the few side effects restrict its extensive clinical application, particularly for deeply buried tumors [11]. Although the near-infrared red (NIR) or multi-photon excitation has been employed to increase the tissue penetration depth of light [12–14], the light source is expensive and bulky, not highly suitable for *in-vivo* and clinical applications [14,15]. Instead of light, ultrasound (US) is used as the stimuli to trigger the production of reactive oxygen species (ROS) by sonosensitizers to kill cancer, that is sonodynamic therapy (SDT) [16–18]. Due to the much higher tissue penetration depth of US, SDT can be applied to treat large tumors or deep-seated tumors [19]. Furthermore, US can be employed precisely to the tumor site for the activation of the sonosensitizers to selectively kill tumor cells without any significant damage to the adjacent normal tissues [20,21].

Metal complexes, such as Pd(II) (WST11), Lu(III) (Lutex), Sn(IV) (Purlytin) and Ru(II) (TLD-1433) complexes were in clinical trial as PDT agents [22,23]. Unfortunately, these metal-based photosensitizers are rarely used in the study of SDT. Among various metal complexes, Ir(III) complexes are widely employed as photosensitizers due to their high photostability, good cellular uptake, and impressive singlet oxygen ($^1O_2$) generation quantum yield [24–26]. In addition, recent work by Sadler *et al.* and our own work showed that Ir(III) complexes could photocatalytically oxidize endogenous coenzyme NADH (1,4-dihydronicotinamide adenine dinucleotide) to disrupt the redox balance in cancer cells and ultimately effect cancer cells death [27,28]. However, most of the Ir(III) complexes are hydrophobic and their photo-chemotherapeutic effects in the hydrophilic environment of cellular systems are greatly reduced [29]. Furthermore, Ir(III) complexes usually exhibit long-term toxicity due to their high uptake and retention in the reticuloendothelial system [30]. Thus, developing a novel Ir(III)-based anticancer agent with appropriate water solubility, good biosafety, and excellent $^1O_2$ generation ability and thereafter extend its application as a SDT agent is highly challenging and yet to be developed.

In recent years, nanotechnology has provided a unique way to improve the aqueous solubility and biosafety of metal-based complexes [31–35]. Ultrasmall luminescent gold nanoparticles (AuNPs)

* Corresponding author.
E-mail address: p.zhang6@szu.edu.cn (P. Zhang).

https://doi.org/10.1016/j.cclet.2021.11.017
1001-8417/

with unique optical properties, multifunctional surface, long blood circulation, high metabolic clearance, and low toxicity have received great interest in biosensing, bioimaging, and therapy [36–38]. Recently, functionalized ultrasmall AuNPs have been used in nanoparticle-based drug delivery systems, such as for doxorubicin (DOX) [39,40], small interfering ribonucleic acid (siRNA) [41], and deoxyribonucleic acid (DNA) delivery [42]. However, ultrasmall AuNPs are rarely studied in the field of SDT. Therefore, combining the ultrasmall AuNPs with an Ir(III) complex is expected to provide a novel nano-platform, which may show significant SDT performance. This hypothesis provides us the basis of the present study.

Herein, we designed and developed a new organometallic Ir(III) complex (Ir1) hybridized ultrasmall gold nanoparticles (AuNPs@Ir1) by using albumin as a bridge. Important results included US-triggered cytotoxicity of AuNPs@Ir1 in cancer cells while being significantly less toxic to normal cell lines in the absence of US irradiation. The oncosis type *in-vitro* cytotoxicity of AuNPs@Ir1 under US exposure was related to its catalytic intracellular NADH oxidation ability and intracellular ROS generation. Moreover, due to the efficient passive retention in tumors post intravenous injection, AuNPs@Ir1 inhibited the growth of the tumors *in-vivo* even up to *ca.* 70%, without any significant toxicity to other organs.

The Ir(III) complex $[Ir(F_2ppy)_2(mqbs)]Cl$ (Ir1) was synthesized in detail in the experimental section and characterized in Supporting information (Figs. S1-S4 in Supporting information). The earlier studies showed that Ir(III) complex could easily bind to albumin [43,44]. Herein we selected the bovine serum albumin (BSA) as the surface coating agent for the synthesis of ultrasmall gold nanoparticles (AuNPs) and then bound with Ir1. The BSA coated AuNPs have been synthesized and purified according to the previous reports [45]. AuNPs showed bright red luminescence with a distinct peak at 630 nm when excited with 365 nm light (Fig. S5 in Supporting information) in water. The TEM imaging indicated that the size of the ultrasmall AuNPs was ~1.4 nm. After the Ir1 hybridization, we developed AuNPs@Ir1 (Synthesis and purification are given in Supporting information, Figs. S6 and S7) with highly uniform morphology and an average diameter of *ca.* 117 nm, a polydispersity index of *ca.* 0.10 in PBS (Figs. 1a and b).

Dynamic light scattering (DLS) measurement showed that the AuNPs@Ir1 was well dispersible in water, phosphate buffer saline (PBS), and RPMI-1640 cell culture medium, giving an average hydrodynamic size of *ca.* 145 nm (Fig. 1d and Fig. S8 in Supporting information). After hybridization with the Ir1, the surface potential of the nanoparticles decreased from −5.8 mV to −38.0 mV (Fig. S9 in Supporting information). The higher negative surface charge probably yields better physical stability [46]. The elemental mapping showed the homogeneous distribution of Au in AuNPs@Ir1, whereas Ir was mainly concentrated in the interior of the nanoparticles (Figs. 1c and e). Furthermore, we used ICP-MS to determine the ratio of Ir/Au in AuNPs@Ir1, and the obtained result showed that the optimal Ir/Au ratio was 9:11 (Fig. S10 in Supporting information). The characteristic absorption bands of Ir1 at ~320 and 420 nm were observed with AuNPs@Ir1, further confirming the successful synthesis of AuNPs@Ir1 (Fig. 1f). In addition, the absorption spectra and hydrodynamic size of AuNPs@Ir1 were almost unchanged over 72 h in the PBS solution or RPMI-1640 cell culture media (Figs. S11 and S12 in Supporting information), suggesting that AuNPs@Ir1 is highly stable under physiological environment.

Circular dichroism (CD) was used to investigate the effect of the self-assemble process on the BSA structure. The CD spectra (Fig. S13 in Supporting information) showed that the formation of AuNPs had a slight effect on the α-helical structure of BSA, but the structure was severely affected after binding with the Ir1. Molecular docking was performed to reveal the binding sites on BSA and associated binding affinities for the Ir1. At first, the geometry of the

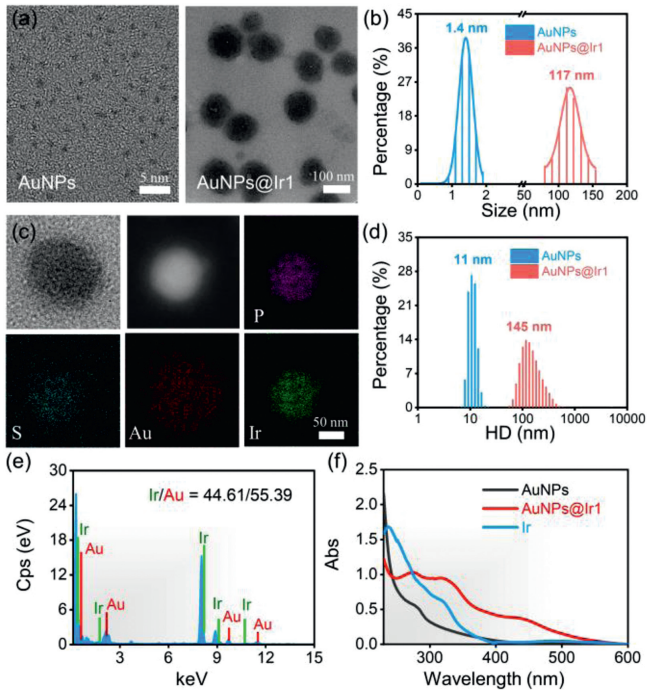

Fig. 1. (a) TEM images of AuNPs and AuNPs@Ir1. (b) The core sizes of AuNPs and AuNPs@Ir1 from the images presented in (a). (c) HAADF-STEM images and elemental mapping of AuNPs@Ir1. (d) DLS of AuNPs and AuNPs@Ir1. (e) EDS of AuNPs@Ir1. (f) Absorption spectra of the Ir1, AuNPs, and AuNPs@Ir1 in water.

Ir1 was optimized in vacuum by density functional theory (DFT) (Fig. S14 in Supporting information). Then the docking of the optimized Ir1 into the prepared rigid structure of the BSA protein was performed using the Autodock Vina software package. As shown in Fig. S15 (Supporting information), BSA was firstly bound to one Ir1 (represented by orange part), and the affinity was the strongest. On the binding surface, BSA interacted with the Ir1 *via* several amino acid residues such as Thr419, Lys504, His509, Ala527 and Glu530. Immediately, BSA was observed to bind with the second and third Ir1 (the green and the pink parts, respectively). These results indicated that BSA has enough possibility to adsorb at least three Ir1 and Ir1 has strong interactions with the BSA to form a micelle-like structure.

To evaluate the sonosensitizer performance of the AuNPs@Ir1, we first evaluated the sono-stability of AuNPs@Ir1. There was almost no change in the UV–vis and emission spectra of AuNPs@Ir1 even after 1 h US irradiation, showing the high sono-stability of the AuNPs@Ir1 (Fig. S16 in Supporting information). 2′,7′-Dichlorodihydrofluorescein diacetate (DCFH-DA), a ROS probe, was employed to detect total ROS generation by US irradiation. After mixing the AuNPs@Ir1 with the DCFH-DA, the fluorescence spectra of the mixture were monitored at different exposure periods of US irradiation (Fig. 2a). The gradual enhancement of the fluorescence intensity at 525 nm of the reaction mixture with increasing US irradiation time indicated the generation of ROS during US irradiation (Fig. 2b). Moreover, we found that the ROS generation ability of AuNPs@Ir1 was comparable to that of the Ir1, while both were higher than the free AuNPs (Fig. S17 in Supporting information). 9,10-Diphenanthraquinone (DPA) is a well-known probe to determine the quantum yield of $^1O_2$ generation, if any [47]. The $^1O_2$ can oxidize DPA to 9,10-diphenanthraquinone dioxide (DPO_2), which has no obvious absorption in the visible region [48]. As revealed in Fig. 2c, the intensity of DPA's characteristic absorption peak at 380 nm significantly decreased with the increase of US irradiation time in the presence of AuNPs@Ir1, suggesting the US-triggered

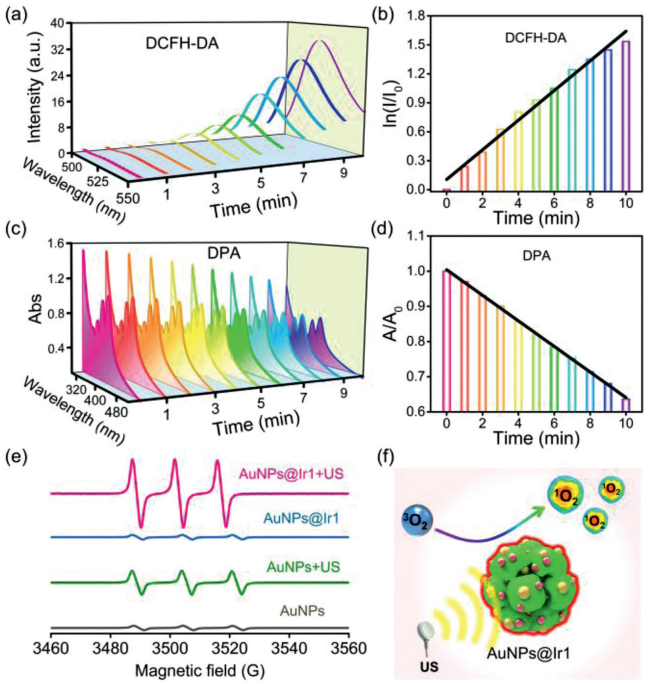

Fig. 2. (a) Time-dependent fluorescence spectra of DCFH-DA indicating ROS generation by AuNPs@Ir1 under US irradiation (0.3 W/cm^2, 3 MHz). (b) Representative plot showing the effect of US irradiation time on the DCFH-DA fluorescence intensity at 525 nm in the presence of AuNPs@Ir1. (c) Time-dependent absorption spectra of DPA indicating $^1O_2$ generation by AuNPs@Ir1 under US irradiation (0.3 W/cm^2, 3 MHz). (d) Representative plot showing the effect of US irradiation time on the DPA absorption at 380 nm in the presence of AuNPs@Ir1. (e) $^1O_2$ generation by AuNPs@Ir1 under US irradiation detected by ESR spectra (0.3 W/cm^2, 3 MHz, 20 min). (f) Schematic illustration of sonosensitizer performance of AuNPs@Ir1.

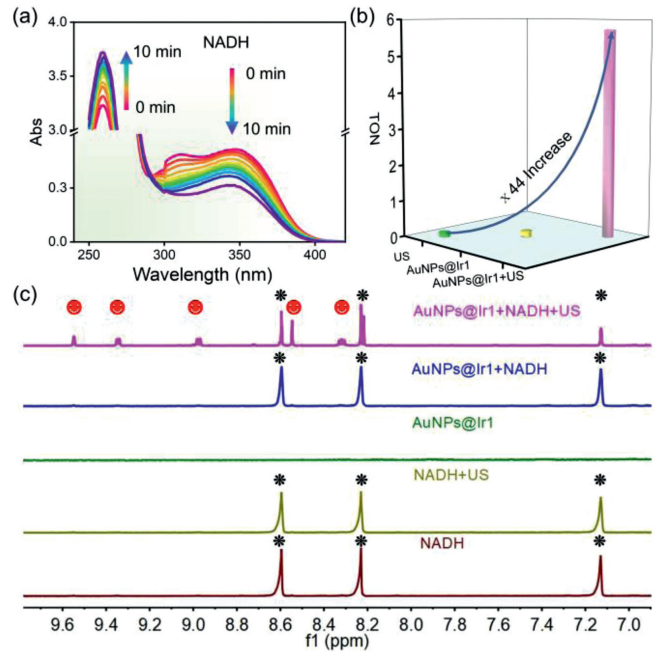

Fig. 3. (a) Sonocatalytic oxidation of NADH by AuNPs@Ir1 (10 μmol/L based on Ir1 complex) in PBS solution under US irradiation tracked by UV–vis spectra. (b) TON values of AuNPs@Ir1 for catalyzing NADH with or without US irradiation. (c) Sonocatalytic oxidation of NADH by AuNPs@Ir1 in D_2O/CD_3OD (1/2, v/v) with US irradiation (0.3 W/cm^2, 3 MHz, 20 min). Peaks labeled with black and red correspond to NADH and NAD$^+$ ^{1}H signals, respectively.

generation of $^1O_2$ by AuNPs@Ir1. The oxidation rate of DPA had a linear correlation with the US irradiation time, and the rate constant of AuNPs@Ir1 (0.036 min^{-1}) was higher than that of AuNPs (Fig. 2d and Fig. S18 in Supporting information). Methylene blue (MB) was used to detect $^{\bullet}$OH generation [49]. The results showed that AuNPs@Ir1, along with the US irradiation, could hardly produce any $^{\bullet}$OH (Fig. S19 in Supporting information). Electron spin resonance (ESR) was employed to directly confirm the nature of the produced ROS. The trapping agents 2,2,6,6-tetramethylpiperide (TEMP) and 5,5-dimethyl-1-pyrroline-*N*-oxide (DMPO) were chosen to trap $^1O_2$ and $^{\bullet}$OH, respectively (Fig. 2e). AuNPs@Ir1 under US irradiation gave the EPR signal only corresponding to the TEMP-$^1O_2$ adduct formation, which again verified that AuNPs@Ir1 had a strong ability to produce $^1O_2$ under US irradiation (Fig. 2f).

NADH is an important coenzyme for mitochondrial functions and redox balance maintenance in living cells [50,51]. The oxidation of NADH to NAD$^+$ can significantly perturb the intracellular redox homeostasis and kill cancer cells effectively [52,53]. Therefore, the sonocatalytic NADH oxidation efficiency of AuNPs@Ir1 was evaluated under US irradiation. As shown in Fig. 3a, in the presence of AuNPs@Ir1, the NADH characteristic absorption at *ca.* 339 nm was decreased, and NAD$^+$ characteristic absorption at *ca.* 259 nm was increased gradually with increasing the time of US irradiation, indicating the sonocatalytic NADH oxidation by AuNPs@Ir1. In contrast, the control groups (NADH + US, NADH + AuNPs@Ir1 without US irradiation) did not give any notable NADH oxidation (Fig. S20 in Supporting information). We found a US irradiation time dependent on first-order kinetics of NADH oxidation. AuNPs@Ir1 gave the sonocatalytic NADH oxidation turnover number (TON) *ca.* 5.73 (Fig. 3b). The sonocatalytic oxidation of NADH by AuNPs@Ir1 was further confirmed by ^{1}H NMR spectroscopy (Fig. 3c). Before US irradiation, the NMR spectroscopy of the reaction mixture of AuNPs@Ir1 (0.1 mmol/L based on Ir1 complex) and NADH (3 mmol/L) remained unchanged. But after irradiation with US for 20 min, five new peaks (at 9.55, 9.34, 8.97, 8.54, and 8.31 ppm) assignable to the protons of NAD$^+$ appeared in the ^{1}H NMR spectra. These results indicated that AuNPs@Ir1 is a good catalyst for sonocatalytic oxidation NADH to NAD$^+$ and could potentially impart intracellular redox imbalance to give cells death.

Adequate cellular internalization of any drugs is necessary to ensure an effective therapeutic effect. The phosphorescence of AuNPs@Ir1 was used to study its intracellular uptake in mouse breast cancer cells (4T1) by confocal laser scanning microscopy (CLSM). In order to study the subcellular localization of AuNPs@Ir1 precisely, we stained the living 4T1 cells with the commercial lysosome targeting dye Lyso-Tracker Green (LTG) after incubation with AuNPs@Ir1. As shown in Fig. 4a, the red intracellular emission of AuNPs@Ir1 significantly merged with the green emission of LTG with a Pearson's colocalization coefficient (PCC) value of 0.85, indicating the specific lysosomes targeting capability of AuNPs@Ir1 in the living 4T1 cells. Furthermore, the cellular uptake of AuNPs@Ir1 was investigated by ICP-MS. AuNPs@Ir1 entered into the 4T1 cells effectively and rapidly with a maximum cell internalization rate constant of 25.9%/10^4 cells after 4 h of incubation. Prolonged incubation resulted in the excretion of AuNPs@Ir1 from the cells (Fig. S21 in Supporting information). The obtained data indicated that AuNPs@Ir1 with good cellular uptake and lysosomes targeting nature might have good application in cancer sonodynamic therapy.

The *in-vitro* SDT efficiency of AuNPs@Ir1 was evaluated by the standard MTT assay. At first, we evaluated the toxicity of the Ir1 and AuNPs@Ir1 against human normal liver cells (L02). Different from the free Ir1 complex, AuNPs@Ir1 did not exhibit any significant toxicity towards normal L02 cells even at high concentration and prolonged incubation for 24 h, indicating the good biosafety of AuNPs@Ir1 (Fig. 4b). Next, we studied the effects of different US

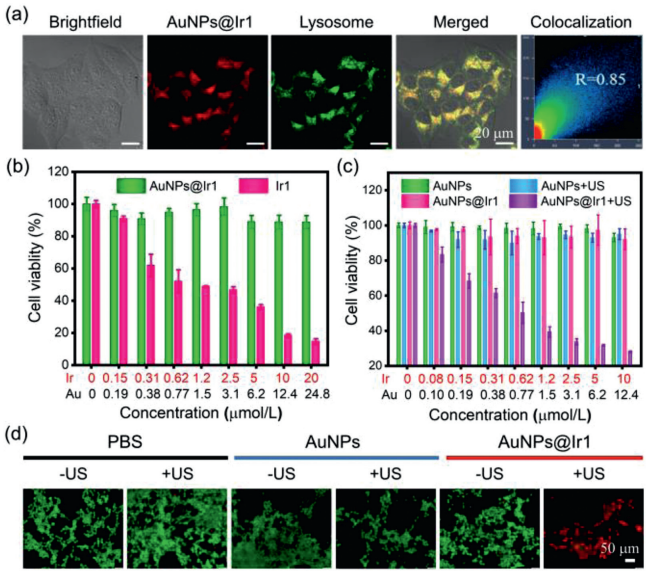

Fig. 4. (a) CLSM images of the living 4T1 cells treated with AuNPs@Ir1 (10 μmol/L based on Ir1, 4 h incubation) and co-stained with LTG (50 nmol/L, 30 min). AuNPs@Ir1: λ_{ex} = 450 nm, λ_{em} = 650 ± 30 nm; LTG: λ_{ex} = 488 nm, λ_{em} = 520 ± 30 nm. (b) Cell viabilities of L02 after incubation with different concentrations of the Ir1 or AuNPs@Ir1. (c) Cell viabilities of 4T1 cells after incubation with different concentrations of AuNPs or AuNPs@Ir1 in the presence or absence of US irradiation (3 MHz, 0.3 W/cm^2, 20 min). (d) CLSM images of 4T1 cells co-stained with calcein AM and PI after different treatments.

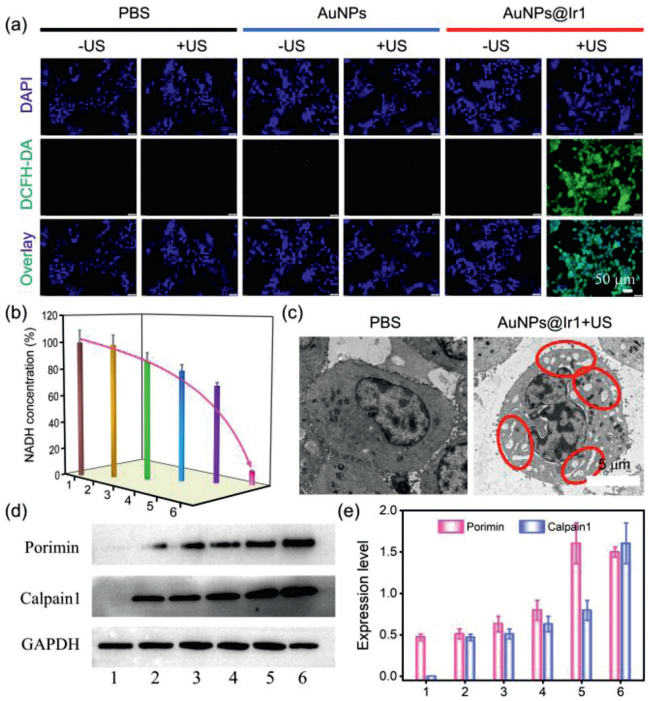

Fig. 5. (a) CLSM images of 4T1 cells stained with DCFH-DA (green) after various treatments. (b) The NADH concentration in 4T1 cells after various treatments. (c) TEM images of 4T1 cells incubated with AuNPs@Ir1 in the presence of or absence of US irradiation. (d) Western blot analysis of Porimin and Calpain1 in 4T1 cells after different treatments. (e) Expression levels of Porimin and Calpain1 in 4T1 cells quantified from (d) [1: PBS, 2: PBS + US, 3: AuNPs, 4: AuNPs + US, 5: AuNPs@Ir1, 6: AuNPs@Ir1 + US]. AuNPs@Ir1: 10 μmol/L based on Ir1; US: 0.3 W/cm^2, 3 MHz, 20 min.

doses on the 4T1 cells. Various US doses were selected by controlling US irradiation power and time. As shown in Fig. S22 (Supporting information), the power of the US above 0.3 W/cm^2 (3 MHz, 20 min) or irradiation time over 25 min (3 MHz, 0.3 W/cm^2), decreased the cell viability in the control group. Based on this experiment, we chose the US dose of 3 MHz, 0.3 W/cm^2, 20 min, which is safe for the cells. Interestingly, under this US dose irradiation, cell viabilities of 4T1 cells continuously decreased as increasing AuNPs@Ir1 concentration (Fig. 4c). The IC_{50} value of AuNPs@Ir1 was *ca.* 0.6 μmol/L based on Ir1. Moreover, the excellent cancer cell killing ability of AuNPs@Ir1 against the 4T1 cells upon US irradiation was also confirmed by calcein AM (live cells) and PI (dead cells) co-staining (Fig. 4d). Overall, the obtained results depicted that AuNPs@Ir1 can be used as a tumor-targeting highly effective SDT agent for cancer treatment as the specific tumorous area will be irradiated by the US, keeping the non-US irradiated normal cells unaffected.

To verify the hypothesis that AuNPs@Ir1 induced cancer cells death by ROS generation on US exposure, DCFH-DA staining was used to know if there is any enhancement of intracellular ROS level in the presence of AuNPs@Ir1 +/– US irradiation (Fig. 5a). Very weak green fluorescence of DCFH-DA was observed after treatment of cells with US alone, AuNPs alone, AuNPs + US or AuNPs@Ir1 alone. In contrast, very strong green fluorescence from DCFH-DA was observed in the AuNPs@Ir1+US treated cells, demonstrating a large amount of cellular ROS production. We also investigated the possibility of cellular NADH depletion by AuNPs@Ir1 upon US exposure (Fig. 5b). After incubation with AuNPs@Ir1, cellular NADH concentration was significantly reduced under US irradiation. These results confirmed that upon US irradiation, AuNPs@Ir1 can kill tumor cells by a dual mechanism of action (i) ROS generation and (ii) NADH oxidation. Till today, such kinds of mechanisms are only known for very few photocatalytic anticancer metal complexes [27]. This report, for the first time, reveals that similar catalytic anticancer agents can be developed not only with photoactive metal complexes but also with US-active nanomaterials.

To classify the mode of cell death in the AuNPs@Ir1 induced by SDT process, CLSM and TEM were used to observe the morphological alterations in the 4T1 cells. On CLSM imaging, we observed cell swelling after AuNPs@Ir1 + US treatment (Fig. S23 in Supporting information). Furthermore, multiple cytoplasmic blebs, nucleus swelling, and nuclear chromatin clumping were detected by TEM (Fig. 5c). The observed morphological changes demonstrated a mode of cell death consistent with the oncosis. We used western blotting to check the level of activated oncosis specific proteins, the Porimin, and Calpain1. As shown in Fig. 5d, in the control group, the expression levels of two proteins were very low. However, after AuNPs@Ir1+US treatment, the expression levels of above two proteins were largely increased (Fig. 5e), indicating that AuNPs@Ir1 significantly upregulates Porimin and Calpain1, and induces cell oncosis.

The interesting *in-vitro* results provided us the backdrop to investigate the antitumor profile of AuNPs@Ir1 at the *in-vivo* level. To study the tumor targeting efficiency of AuNPs@Ir1, 4T1 tumors bearing mice (Balb/c) were used as a model system, and the biodistribution of the AuNPs@Ir1 in the mice at different time points was quantified after intravenous (i.v.) injection (1, 12, 24 and 48 h) by measuring the content of iridium using ICP-MS (Fig. S24 in Supporting information). The high tumor targeting efficiency of AuNPs@Ir1 was clearly observed, which verifies the good uptake of AuNPs@Ir1 in tumors *via* enhanced permeability and retention. The highest tumor localization was observed after 12 h post injection and was quantified to be *ca.* 8.18%ID/g, confirming the efficient tumor accumulation of AuNPs@Ir1.

Encouraged by the excellent *in-vivo* tumor accumulation and *in-vitro* sonodynamic performance of AuNPs@Ir1, we used 4T1 tumors bearing mice model to study the *in-vivo* antitumor profile of AuNPs@Ir1 upon US irradiation (Figs. 6a and b). Animal care

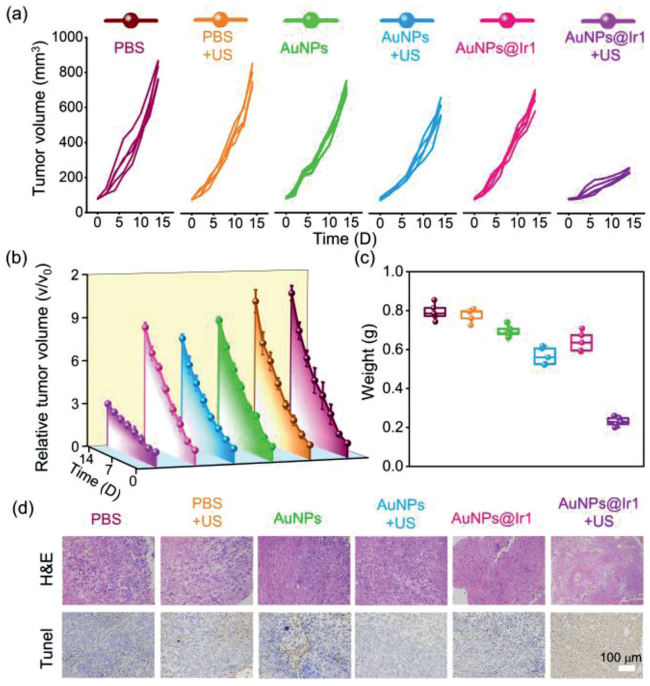

Fig. 6. (a) The individual and (b) average tumor growth curves in mice after different treatments, including PBS, PBS + US, AuNPs, AuNPs + US, AuNPs@Ir1, and AuNPs@Ir1 + US. (c) Average tumor weights of mice at 14 days post treatments. (d) Microscopy photos of H&E and TUNEL stained tumor slices.

and experiments were performed in accordance with the Animal Research Ethics Committee of Shenzhen University, permit number AEWC-201,412,003. The mice were randomly divided into six groups ($n = 5$): (1) PBS; (2) PBS + US; (3) AuNPs; (4) AuNPs + US; (5) AuNPs@Ir1; (6) AuNPs@Ir1 + US. At 12 h post i.v. injection of AuNPs or AuNPs@Ir1, the tumors were subjected to US irradiation (3 MHz, 0.3 W/cm^2, 20 min). After the treatment, the tumor growth of each group of mice was monitored by digital caliper every two days. The PBS, PBS + US, AuNPs, AuNPs + US and AuNPs@Ir1 groups showed similar and negligible antitumor efficiency, indicating that only US or only AuNPs@Ir1 has no obvious effect on tumor growth. The tumor growth of the SDT group (AuNPs@Ir1 + US) was remarkably suppressed (Fig. 6c). The tumor growth inhibition of *ca.* 71.4%, suggested the excellent *in-vivo* SDT performance of AuNPs@Ir1.

The excellent SDT performance was also observed from the hematoxylin and eosin (H&E) staining and TdT-mediated dUTP nick-end labeling (TUNEL) staining of tumor slices after various treatments (Fig. 6d). In line with the above-mentioned tumor growth inhibition results, the AuNPs@Ir1 + US group showed the most severe tissue damage of the tumor tissue, as was evident from the large spaces formation among tumor cells as well as severe nucleus shrinkage, plasmatorrhexis, and karyorrhexis. In contrast, the other five groups showed no obviously tissue damage confirmed by both H&E and TUNEL staining slices. In addition, the *in-vivo* ROS staining of the tumor slices was carried out to evaluate the ROS levels in the tumor site *in-vivo*. Compared with the weak green fluorescence of the tumor slices from PBS, PBS + US, AuNPs, AuNPs + US and only AuNPs@Ir1 groups, the AuNPs@Ir1 + US group gave significantly strong green fluorescence, demonstrating that AuNPs@Ir1 generates a significant amount of ROS only after US irradiation in tumors (Fig. S25 in Supporting information). The above results confirm that AuNPs@Ir1 is a highly effective sonosensitizer for SDT of cancer. As the *in-vivo* biosafety is one of the most important prerequisites for drug development and clinical use, we studied the histological changes of major organs, including heart, liver, spleen, lung and kidney, after 14 days of AuNPs@Ir1 + US treatment by H&E staining (Fig. S26 in Supporting information). No evident organ damages and inflammations, indicating that AuNPs@Ir1 has highly *in-vivo* biosafety. The overall *in-vivo* studies indicate that the highly bio-compatible AuNPs@Ir1 with remarkable antitumor effect is a good candidate for the clinical trial.

In summary, we have developed a facile and versatile method using BSA-coated AuNPs as structural units to synthesize AuNPs@Ir1 assemblies, taking the advantage of hydrophobic interaction between BSA and the newly developed Ir(III) complex, the Ir1. We evaluated the effectivity of AuNPs@Ir1 as a sonosensitizer for sonodynamic therapy of cancer, an emerging alternative of photo-activated cancer therapy (PACT) with the promises to overcome the drawbacks of PACT. The surface of AuNPs@Ir1 was capped by the hydrophilic domain of BSA, affording excellent aqueous solubility, one of the desire factors of drug development. The highly *in-vitro* biocompatible AuNPs@Ir1 serves as a potent sonosensitizer to generate intracellular $^1O_2$ as well as an excellent sonocatalyst for intracellular NADH oxidation. The US-triggered $^1O_2$ generation and NADH oxidation by AuNPs@Ir1 resulted in excellent *in-vitro* anticancer activity by disrupting the redox balance in cancer cells, ultimately produced oncosis as the mode of cancer cells death. Remarkably, we were successful to translate our *in-vitro* anticancer effect to *in-vivo* and AuNPs@Ir1 achieved highly efficient SDT performance to inhibit *in-vivo* tumors growth, due to the efficient tumor accumulation of AuNPs@Ir1 after i.v. injection. Significantly, AuNPs@Ir1 did not induce any notable toxicity to the organs of treated mice during the treatment process indicating very high *in-vivo* biosafety of AuNPs@Ir1.

In literature, several gold nanoparticles are reported to show SDT performance with the US power of 0.5–30 W/cm^2 [54–57]. Compared to those reports, here, we have achieved highly efficient SDT with lower power (0.3 W/cm^2) of US irradiation. Overall, AuNPs@Ir1 with excellent *in-vivo* biosafety and promising US-triggered *in-vivo* anticancer activity has the potential to be studied as a highly efficient sonosensitizer for clinical sonodynamic therapy. Moreover, this work is expected to open up a new avenue of SDT, an emerging and potential alternative of cancer phototherapy by metal-based drugs.

Declaration of competing interest

The authors declared that they do not have any commercial or associative interest that represents a conflict of interest in connection with the work submitted.

Acknowledgments

We appreciate the financial support of the National Natural Science Foundation of China (NSFC, Nos. 22077085, 22007104), the Project of the Natural Science Foundation of Guangdong Province (No. 2019A1515011958) and the Science and Technology Foundation of Shenzhen (No. JCYJ20190808153209537) and DST, the Government of India (No. DST/INSPIRE/04/2019/000492). We thank Mrs. Shaoxia Liang for ICP-MS measurement from PerkinElmer, Inc. Guangzhou, China. We appreciate the Instrumental Analysis Center of Shenzhen University.

Supplementary materials

Supplementary material associated with this article can be found, in the online version, at doi:10.1016/j.cclet.2021.11.017.

References

[1] R.L. Siegel, K.D. Miller, A. Jemal, CA-Cancer J. Clin. 69 (2019) 7–34.
[2] S. Liang, X. Deng, P. Ma, et al., Adv. Mater. 32 (2020) e2003214.
[3] H.Z. Deng, Z.J. Zhou, W.J. Yang, et al., Nano Lett. 20 (2020) 1928–1933.
[4] L.S. Lin, J.B. Song, L. Song, et al., Angew. Chem. Int. Ed. 57 (2018) 4902–4906.
[5] H. Chen, Z. Liu, O. Jiang, et al., Giant 8 (2021) 100073.
[6] A. Grzybowski, K. Pietrzak, Clin. Dermatol. 30 (2012) 451–455.
[7] D. Dolmans, D. Fukumura, R.K. Jain, Nat. Rev. Cancer 3 (2003) 380–387.
[8] S. Monro, K.L. Colon, H.M. Yin, et al., Chem. Rev. 119 (2019) 797–828.
[9] C. Li, Y. Wang, Y. Lu, et al., Chin. Chem. Lett. 31 (2020) 1183–1187.
[10] L. Shen, T. Zhou, Y. Fan, et al., Chin. Chem. Lett. 31 (2020) 1709–1716.
[11] D.F. Costa, L.P. Mendes, V.P. Torchilin, Adv. Drug Deliv. Rev. 138 (2019) 105–116.
[12] S. Kuang, L. Sun, X. Zhang, et al., Angew. Chem. Int. Ed. 59 (2020) 20697–20703.
[13] J. Karges, S. Kuang, F. Maschietto, et al., Nat. Commun. 11 (2020) 3262.
[14] F. Heinemann, J. Karges, G. Gasser, Acc. Chem. Res. 50 (2017) 2727–2736.
[15] J. Hess, H.Y. Huang, A. Kaiser, et al., Chem. Eur. J. 23 (2017) 9888–9896.
[16] N. Yumita, Y. Iwase, K. Nishi, et al., Theranostics 2 (2012) 880–888.
[17] P. Huang, X. Qian, Y. Chen, et al., J. Am. Chem. Soc. 139 (2017) 1275–1284.
[18] X. Pan, W. Wang, Z. Huang, et al., Angew. Chem. Int. Ed. 59 (2020) 13557–13561.
[19] X. Qian, Y. Zheng, Y. Chen, Adv. Mater. 28 (2016) 8097–8129.
[20] F. Gong, L. Cheng, N. Yang, et al., Nat. Commun. 11 (2020) 3712.
[21] X. Wang, X. Zhong, L. Bai, et al., J. Am. Chem. Soc. 142 (2020) 6527–6537.
[22] C. Imberti, P. Zhang, H. Huang, et al., Angew. Chem. Int. Ed. 59 (2020) 61–73.
[23] X. Wang, X. Wang, S. Jin, et al., Chem. Rev. 119 (2019) 1138–1192.
[24] C. Jin, F. Liang, J. Wang, et al., Angew. Chem. Int. Ed. 59 (2020) 15987–15991.
[25] L. Hao, Z.W. Li, D.Y. Zhang, et al., Chem. Sci. 10 (2019) 1285–1293.
[26] P.Y. Zhang, C.K.C. Chiu, H.Y. Huang, et al., Angew. Chem. Int. Ed. 56 (2017) 14898–14902.
[27] H. Huang, S. Banerjee, K. Qiu, et al., Nat. Chem. 11 (2019) 1041.
[28] C. Huang, C. Liang, T. Sadhukhan, et al., Angew. Chem. Int. Ed. 60 (2021) 9474–9479.
[29] Q. Yang, H. Jin, Y. Gao, et al., ACS Appl. Mater. Interfaces 11 (2019) 15417–15425.
[30] S. Yi, Z. Lu, J. Zhang, et al., ACS Appl. Mater. Interfaces 11 (2019) 15276–15289.
[31] S.M. King, S. Claire, R.I. Teixeira, et al., J. Am. Chem. Soc. 140 (2018) 10242–10249.
[32] P. Zhang, J. Wang, H. Huang, et al., Biomaterials 35 (2014) 9003–9011.
[33] J. Xie, C. Liang, S. Luo, et al., ACS Appl. Mater. Interfaces 13 (2021) 27934–27944.
[34] N. Kong, X. Ji, J. Wang, et al., Nano Lett. 20 (2020) 3943–3955.
[35] J. Huang, X. You, P. Xin, et al., Chin. Chem. Lett. 32 (2021) 1737–1742.
[36] Y. Tan, K. He, B. Tang, et al., ACS Nano 14 (2020) 13975–13985.
[37] Y. Chen, L. Li, L. Gong, et al., Adv. Funct. Mater. 29 (2019) 1806945.
[38] J. Liu, M. Yu, C. Zhou, et al., J. Am. Chem. Soc. 135 (2013) 4978–4981.
[39] C. Peng, J. Xu, M. Yu, et al., Angew. Chem. Int. Ed. 58 (2019) 8479–8483.
[40] C. Peng, M. Yu, J.T. Hsieh, et al., Angew. Chem. Int. Ed. 58 (2019) 12076–12080.
[41] Y. Lei, L. Tang, Y. Xie, et al., Nat. Commun. (2017) 15130.
[42] Y. Sun, D. Wang, Y. Zhao, et al., Nano Res. 11 (2018) 2392–2404.
[43] P. Zhang, H. Huang, S. Banerjee, et al., Angew. Chem. Int. Ed. 58 (2019) 2350–2354.
[44] Y. Wang, H. Huang, G. Chen, et al., Chem. Commun. 54 (2018) 3282–3285.
[45] J. Xie, Y. Zheng, J.Y. Ying, J. Am. Chem. Soc. 131 (2009) 888–889.
[46] D. Segets, R. Marczak, S. Schäfer, et al., ACS Nano 5 (2011) 4658–4669.
[47] J. Zhao, J. Fei, C. Du, et al., Chem. Commun. 49 (2013) 10733–10735.
[48] K.Y. Lu, P.Y. Lin, E.Y. Chuang, et al., ACS Appl. Mater. Interfaces 9 (2017) 5158–5172.
[49] H.M. Dao, I. Husain, V.K. Shankar, et al., Chem. Commun. 56 (2020) 12017–12020.
[50] J.F. Turrens, A. Boveris, Biochem. J. 191 (1980) 421–427.
[51] S. Rajagopalan, S. Kurz, T. Munzel, et al., J. Clin. Invest. 97 (1996) 1916–1923.
[52] Z. Liu, R.J. Deeth, J.S. Butler, et al., Angew. Chem. Int. Ed. 52 (2013) 4194–4197.
[53] S. Betanzos-Lara, Z. Liu, A. Habtemariam, et al., Angew. Chem. Int. Ed. 51 (2012) 3897–3900.
[54] V.G. Deepagan, D.G. You, W. Um, et al., Nano Lett. 16 (2016) 6257–6264.
[55] Y. Cao, T. Wu, W. Dai, H. Dong, X. Zhang, Chem. Mater. 31 (2019) 9105–9114.
[56] F. Gao, G. He, H. Yin, et al., Nanoscale 11 (2019) 2374–2384.
[57] J. Ouyang, L. Deng, W. Chen, et al., Chem. Commun. 54 (2018) 2874–2877.